Dependence of mechanical and thermoelectric properties of Mg_2Si-Sn nanocomposites on interface density

Gwansik Kim [a], Hwijong Lee [a], Hyun Jun Rim [a], Jeongmin Kim [a], Kwanlae Kim [a], Jong Wook Roh [b], Soon-Mok Choi [c], Byung-Wook Kim [d], Kyu Hyoung Lee [a, **], Wooyoung Lee [a, *]

[a] Department of Materials Science and Engineering, Yonsei University, Seoul 03722, South Korea
[b] School of Nano & Materials Science and Engineering, Kyungpook National University, Gyeongsangbuk-do 37224, South Korea
[c] School of Energy, Materials and Chemical Engineering, Korea University of Technology and Education, Cheonan 31253, South Korea
[d] Research and Development Division, Hyundai Motor Company, Uiwang 16082, South Korea

ABSTRACT

We prepared Sn nanoparticle-embedded $Mg_{1.96}Al_{0.04}Si_{0.97}Bi_{0.03}$ nanocomposites and measured their thermoelectric properties and fracture toughness to elucidate the trade-off relationship between thermoelectric and mechanical properties. When Sn nanoparticles (50–150 nm) were introduced at the grain boundaries of the thermoelectric $Mg_{1.96}Al_{0.04}Si_{0.97}Bi_{0.03}$ matrix, the fracture toughness improved because of the inhibition of crack propagation. However, the power factor deteriorated due to the decrease in carrier mobility. We found that interface (between thermoelectric matrix and nanoparticles) density is a critical factor to determine the mechanical properties as well as thermoelectric transport properties. Optimized values of figure of merit (~0.66 @ 873 K) and fracture toughness (1.10 MPa m$^{1/2}$) were obtained for 0.9 vol % Sn nanoparticle-embedded $Mg_{1.96}Al_{0.04}Si_{0.97}Bi_{0.03}$ nanocomposite.

© 2018 Elsevier B.V. All rights reserved.

1. Introduction

Silicide-based thermoelectric (TE) materials are promising candidates for mid-to-high temperature power generation applications, especially automotive TE generators (ATEGs), due to their light weight, high conversion efficiency, and abundance of constituent elements. Recently, researches on the development of silicide-based ATEG systems including materials, modules, and assemblies have been extensively carried out to ensure economic feasibility (efficiency and lifetime) and to improve fuel efficiency of vehicles [1].

The first prerequisite for commercialization of ATEGs is high power generation efficiency ($\eta = \left(\frac{T_H - T_C}{T_H}\right) \cdot \frac{\sqrt{1+ZT_{avg}}-1}{\sqrt{1+ZT_{avg}}+(T_C/T_H)}$), which is directly determined by the performance of the TE material, ZT as represented by the following equation:

$$ZT = \frac{\sigma S^2}{\kappa_{tot}} T$$

where, ZT (dimensionless figure of merit) is determined by the electrical conductivity (σ), Seebeck coefficient (S), and thermal conductivity (κ_{tot}) at a given absolute temperature (T).

In the case of n-type Mg_2Si prepared by a pressure induced sintering process such as hot pressing (HP) and spark plasma sintering (SPS), ZT values (~1.0) have been achieved to a level suitable for commercialization [2]. When we calculated the power generation efficiency, the efficiency was ~10% ($\Delta T = 400$ K).

The second essential factor for commercialization of ATEGs is high mechanical reliability to ensure sufficient lifetime (>50,000 h). However, mechanical properties, especially fracture toughness, of Mg_2Si-based compounds are relatively lower (0.4–0.8 MPa m$^{1/2}$), even in highly dense spark plasma sintered bulks (>97% relative density) [3,4], than those of other TE materials (higher manganese silicide (SPS): 1.63 MPa m$^{1/2}$, skutterudite (SPS): 1.0–1.5 MPa m$^{1/2}$, and half-Heusler (HP): 1.8–2.2 MPa m$^{1/2}$) [5–8]. This indicates that silicide-based TE materials may fail under the operating conditions because of thermal and mechanical stress generated by the high

temperature difference between the two ends of the TE module. To address this issue, studies on improving the mechanical properties of silicides have been carried out by incorporating nanoscale ceramics (SiC nanoparticles and nanowires) with a high fracture toughness [3,9].

In our previous study, we investigated the effect of several metal nanoparticles (Al, Cu, and Sn) on the fracture toughness and the TE properties of $Mg_{1.96}Al_{0.04}Si_{0.97}Bi_{0.03}$ by preparing metal nanoparticle-embedded nanocomposites using nanometal decoration and SPS processes [10]. Nanocomposites with well dispersed metal nanoparticles (~150 nm) at the grain boundaries were fabricated using the above method. Interestingly, the fracture toughness was improved by approximately 35% in the presence of metal nanoparticles at the grain boundaries, suggesting that crack propagation could be effectively deflected at the interfaces between Mg_2Si matrix and metal nanoparticles. However, the electronic transport properties, especially carrier mobility, were significantly deteriorated because of intensified electron scattering. Thus, the ZT values showed a trade-off relationship with the fracture toughness. On the other hand, the thermal conductivity of nanocomposite was reduced by embedding metal nanoparticles due to the intensified phase boundary phonon scattering, thereby hindering phonon transport through the matrix; however, according to Maxwell's equation, the thermal conductivity of the nanocomposite should increase because of the high thermal conductivity of the metal nanoparticles. These results suggest that the design rules for Mg_2Si-based nanocomposites with high TE and mechanical properties of Mg_2Si-based compounds are very complicated.

In the present study, we prepared nanocomposites with a controlled amount of Sn nanoparticles (~150 nm) by nanometal decoration and SPS. We measured their TE transport properties and fracture toughness values to quantitatively investigate the effect of Sn nanoparticles on the trade-off relationship between the two material properties. The results indicated that the key factor to realize simultaneously enhanced TE and mechanical properties is enlargement of interface density using a controlled volume fraction of Sn nanoparticles. This implies that the control of distribution, size, and morphology of the nanophases is important to overcome the trade-off between TE performance and mechanical properties.

2. Experimental

$Mg_{1.96}Al_{0.04}Si_{0.97}Bi_{0.03}$ powders were prepared by up-scaled solid state reaction synthesis technique. The details of the processing conditions are available in our previous reports [2,11]. A simple mix-and-heat process was used to decorate Sn nanoparticles onto the surface of $Mg_{1.96}Al_{0.04}Si_{0.97}Bi_{0.03}$ powders (Fig. 1 (a)) [12–14]. For this, hybrid powders of stannous acetate ($(CH_3COO)_2Sn$) and $Mg_{1.96}Al_{0.04}Si_{0.97}Bi_{0.03}$ were prepared by high-energy ball milling (8000D, SPEX, USA) for 5 min. Subsequently, the powders were heat-treated at 473 K for 3 h under a mixed gas atmosphere (95% Ar and 5% H_2) to remove CH_3COO, considering the melting point of Sn (~505 K). Stannous acetate was added at the fraction of 3–20 wt %, and the remaining Sn nanoparticles fraction was 0.3–2.4 vol % in the surface of the $Mg_{1.96}Al_{0.04}Si_{0.97}Bi_{0.03}$ powders, assuming that the acetate group (CH_3COO) was completely removed through the reduction heat treatment.

Disc-type bulks were fabricated by SPS at 1023 K and 70 MPa for 5 min. All the samples exhibited high relative densities; 97–99% of the theoretical density. The microstructures of the sintered bulks were studied by scanning electron microscopy (SEM, JEOL-7800F, JEOL Ltd., Japan). The temperature dependences of the electrical conductivity (σ) and the Seebeck coefficient (S) were evaluated in the range of 300–873 K using a TE properties measuring system
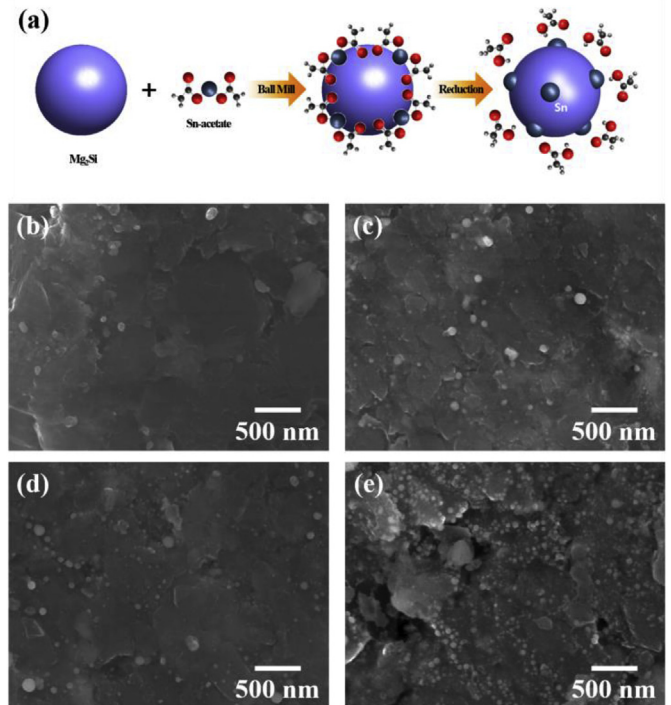

Fig. 1. (a) Schematic diagram of the mix-and-heat process, and SEM images of the hybrid powders of $Mg_{1.96}Al_{0.04}Si_{0.97}Bi_{0.03}$ and Sn nanoparticles with (b) 0.3, (c) 0.9, (d) 1.2, and (e) 2.4 vol % Sn.

(ZEM-3, ULVAC, Japan). Hall effect was measured under a magnetic field of 1 T in the van der Pauw configuration, and the carrier concentration (n_c) and the carrier mobility (μ_{Hall}) were estimated using a one-band model at 300 K. The κ_{tot} values were calculated using the equation $\kappa_{tot} = \rho_s \cdot C_p \cdot \lambda$, where ρ_s is the density, C_p is the specific heat capacity, and λ is the thermal diffusivity. The laser flash method (Netszch LFA-457, Germany) and differential scanning calorimetry (DSC 8000, Perkin Elmer, USA) were used to measure λ and C_p as a function of temperature under vacuum conditions.

A Vickers hardness tester (HM-101, Mitutoyo, Japan) was used to measure the Vickers hardness and radial crack length at a load of 2.942 N and a dwell time of 10 s. Then, the fracture toughness (K_{Ic}) was calculated using the equation:

$$K_{Ic} = \chi \left(\frac{E}{H} \right)^{1/2} \frac{P}{a^{3/2}}$$

where P, E, H, and a are the applied load, Young's modulus, Vickers hardness, and radial crack length, respectively measured from the center of the indent, and χ is the calibration constant taken to be 0.016 ± 0.004 [15].

3. Results and discussion

In thermoelectrics, engineering of the microstructure is one of the key factors to enhance the mechanical as well as the TE properties. Especially, in nanocomposite TE materials, the microstructural characteristics, such as grain size of the TE matrix, and the morphology, size, and distribution of nanoparticles are considered as important material design parameters. In this regard, we analyzed the microstructure evolution of the TE nanocomposite of Sn nanoparticle-embedded $Mg_{1.96}Al_{0.04}Si_{0.97}Bi_{0.03}$ prepared by nanometal decoration and SPS processes. The SEM images of the Sn nanoparticles decorated $Mg_{1.96}Al_{0.04}Si_{0.97}Bi_{0.03}$ hybrid powders are

shown in Fig. 1 (b)−(e). Sn nanoparticles with sizes ranging from 50 to 150 nm are clearly observed in all the samples, and the number of Sn nanoparticles increases with the Sn content. No decrease in the size of the Sn nanoparticles was observed with change in the heat treatment conditions (time (1−10 h), heating rate (1−10 K/min), and temperature (423−473 K)) of the nanometal decoration process.

To analyze the microstructural changes caused by the SPS compaction process, the fractured surfaces of the sintered bulks of 0.3−2.4 vol % Sn nanoparticle-embedded $Mg_{1.96}Al_{0.04}Si_{0.97}Bi_{0.03}$ were also studied by SEM (Fig. 2). Interestingly, two features are observed in the fractured surfaces of the nanocomposites. First, the grain size of the nanocomposites gradually decreases from 3 (Mg_2Si) [2] to 0.5 μm (2.4 vol % Sn nanoparticle-embedded Mg_2Si) as the amount of Sn nanoparticles increases due to the suppression of grain growth. This feature is considered to be related to the mechanical properties as well as the TE properties of the nanocomposites. In our previous report [2], it was confirmed that a decrease in the grain size had a detrimental effect on the TE properties (decreased carrier mobility). Moreover, MgO formed by the reduced grain size can affect the electronic transport properties. MgO can be serious to the reduction of mobility, as can be seen in the previous report [16]. During sintering process, the grain growth was suppressed by the Sn nanoparticles at grain boundaries. The increased interfaces cause the formation of MgO and increase the volume fraction of MgO. Thus, the grain growth inhibition by Sn nanoparticles is expected to have a negative effect on the TE properties mainly because of the decreased mobility. Second, nearly monodispersed Sn nanoparticles with an average size of ~100 nm were observed in the sintered nanocomposites (0.3−0.9 vol % Sn), and they are embedded at the grain boundaries (Fig. 2). However, when the amount of Sn nanoparticles is higher than 1.2 vol %, agglomeration of nanoparticles is clearly observed at the grain boundaries. The reason for the monodispersed behavior observed in the sintered bulks with 0.3−0.9 vol % Sn nanoparticles can be attributed to the increased interface density benefiting from the suppressed grain growth in the presence of Sn nanoparticles. Thus, the interface density as a key factor that determines the mechanical and the TE properties of nanocomposites was estimated from the SEM images (Fig. 2) and the values are listed in Table 1. We estimated the surface area of the nanoparticles as the interface density, assuming that the nanoparticles were two-dimensional circular particles.

We investigated Sn content and interface density dependences of the fracture toughness, as shown in Fig. 3(a) and (b), and found that the fracture toughness showed a more prominent dependency with the interface density due to the agglomeration of the Sn nanoparticles at higher Sn contents. The interface density dependence of the fracture toughness shows a monotonic increase, similar to that observed in nanocomposites [17]. On the other hand, all the nanocomposite samples exhibited the improved fracture toughness compared to the pristine sample (~0.82 MPa m$^{1/2}$). Especially, 0.9 vol % Sn nanoparticle-embedded nanocomposite exhibited a 35% enhanced fracture toughness (~1.10 MPa m$^{1/2}$), and the maximum fracture toughness was ~1.22 MPa m$^{1/2}$ (2.4 vol % Sn nanoparticle-embedded sample). The effect of the grain size on Vickers hardness and Young's modulus is not dominant at present grain size level. Thus, the improved fracture toughness of the nanocomposites was induced by the high fracture toughness of the Sn nanoparticles at the grain boundaries, which can inhibit crack propagation.

Next, we measured temperature and interface density dependence of the TE properties. The electronic transport properties as a function of temperature for the pristine sample and the Sn nanoparticle-embedded nanocomposites are shown in Fig. 4(a) and (b). In the whole measured temperature range, all the nanocomposites exhibit lower σ values than that of the pristine sample, and the σ values of the Sn nanoparticle-embedded nanocomposites were reduced by increasing the Sn content. To clarify this, the n_c and the μ_{Hall} values were calculated by estimating one-band model, and the results are shown in Table 1. The n_c values of all the nanocomposites are similar (9.30×10^{19}−9.96×10^{19} cm^{-3}) and
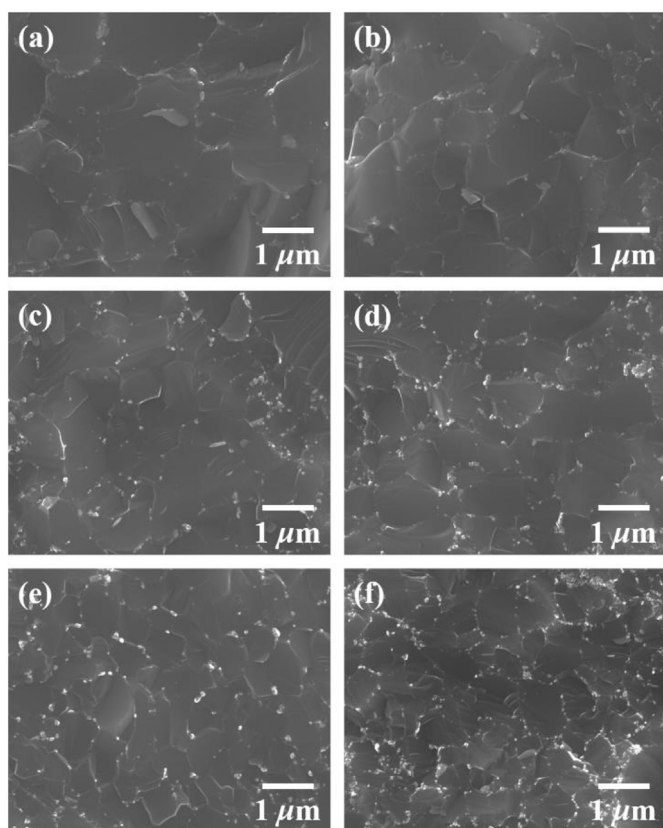

Fig. 2. SEM images of the fractured surfaces of the nanocomposites prepared with (a) 0.3, (b) 0.6, (c) 0.9, (d) 1.2, (e) 1.8, and (f) 2.4 vol % Sn.

Table 1
Room temperature electronic transport parameters and interface density of Sn nanoparticle-embedded $Mg_{1.96}Al_{0.04}Si_{0.97}Bi_{0.03}$ samples.

	Interface density (cm^2 cm^{-3})	σ (S m^{-1})	S (μV K^{-1})	n_c (cm^{-3})	μ_{Hall} (cm^2 V^{-1} s^{-1})
$Mg_{1.96}Al_{0.04}Si_{0.97}Bi_{0.03}$	0	122596.24	−99.78	9.27×10^{19}	81.4
$Mg_{1.96}Al_{0.04}Si_{0.97}Bi_{0.03}$ + 0.3 vol % Sn	789	53997.40	−97.7	9.42×10^{19}	35.3
$Mg_{1.96}Al_{0.04}Si_{0.97}Bi_{0.03}$ + 0.6 vol % Sn	1475	49329.00	−93.0	9.52×10^{19}	31.9
$Mg_{1.96}Al_{0.04}Si_{0.97}Bi_{0.03}$ + 0.9 vol % Sn	1901	37678.63	−99.2	9.67×10^{19}	24.0
$Mg_{1.96}Al_{0.04}Si_{0.97}Bi_{0.03}$ + 1.2 vol % Sn	2195	29100.64	−99.0	9.96×10^{19}	18.0
$Mg_{1.96}Al_{0.04}Si_{0.97}Bi_{0.03}$ + 1.8 vol % Sn	2673	24135.20	−100.6	9.30×10^{19}	16.0
$Mg_{1.96}Al_{0.04}Si_{0.97}Bi_{0.03}$ + 2.4 vol % Sn	3076	16360.17	−104.3	9.33×10^{19}	10.8
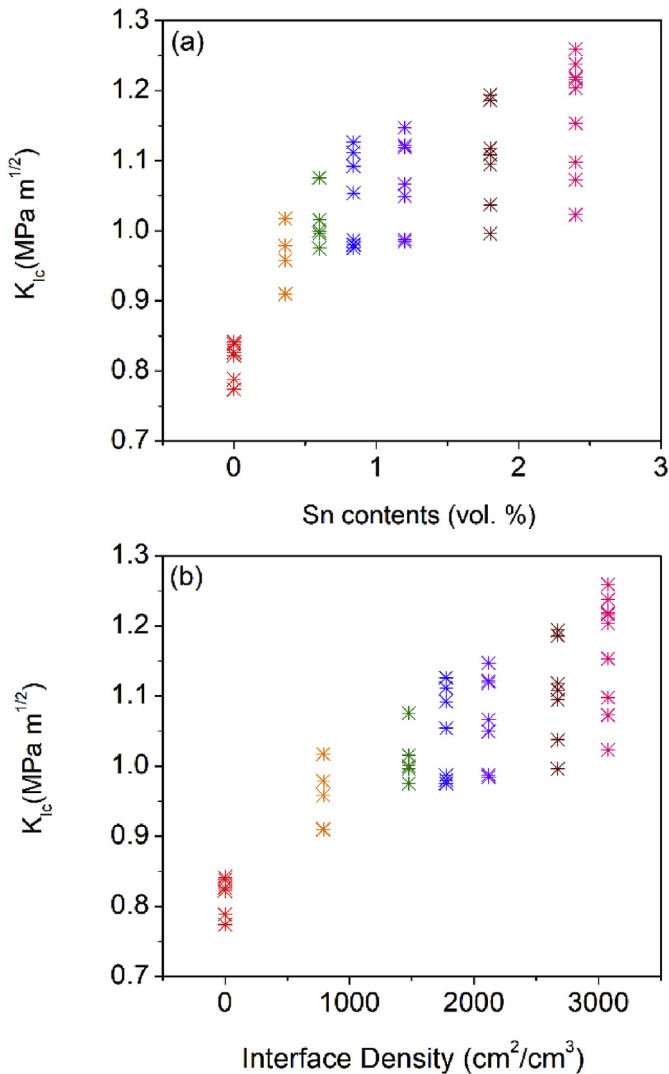
Fig. 3. (a) Sn content and (b) interface density dependence of the fracture toughness.

Fig. 4. Temperature dependences of (a) electrical conductivity and (b) Seebeck coefficient of Sn nanoparticle-embedded $Mg_{1.96}Al_{0.04}Si_{0.97}Bi_{0.03}$ samples. The inset in (b) shows the temperature dependence of power factor.

close to that of the pristine sample (9.27×10^{19} cm^{-3}), indicating that the reduction in the σ values with introduction of Sn nanoparticles is due to the significant decrease in μ_{Hall}. As shown in Table 1, the μ_{Hall} values of all the nanocomposites (10.8–35.3 cm^2 V^{-1} s^{-1}) were much lower than that of the pristine sample (81.4 cm^2 V^{-1} s^{-1}) because of intensified electron scattering by the Sn nanoparticles. The decrease in μ_{Hall} is also related to the MgO, induced by the decrease in the grain size of the samples at higher Sn contents (Fig. 2). Whereas, the S values of all the samples were almost the same because of the similar n_c values. As a result, the power factor (σS^2) values of the nanocomposites (1.51–2.20 mW m^{-1} K^{-2} at 873 K) were lower than that of the pristine sample (2.72 mW m^{-1} K^{-2} at 873 K).

The temperature dependence of κ_{tot} of all the samples is shown in Fig. 5(a). The κ_{tot} values of Sn nanoparticle-embedded nanocomposites (3.89–4.41 W m^{-1} K^{-1} at 373 K and 2.53–2.84 W m^{-1} K^{-1} at 873 K) were lower than those of the pristine sample (5.06 W m^{-1} K^{-1} at 373 K and 2.89 W m^{-1} K^{-1} at 873 K) mainly because of the decrease in electronic contribution by the reduced electron mobility. Interestingly, the κ_{tot} values of the nanocomposites decreased up to a Sn content of 0.9 vol %, and gradually increased thereafter. To clarify this, we calculated the lattice thermal conductivity (κ_{lat}), which is estimated by subtracting
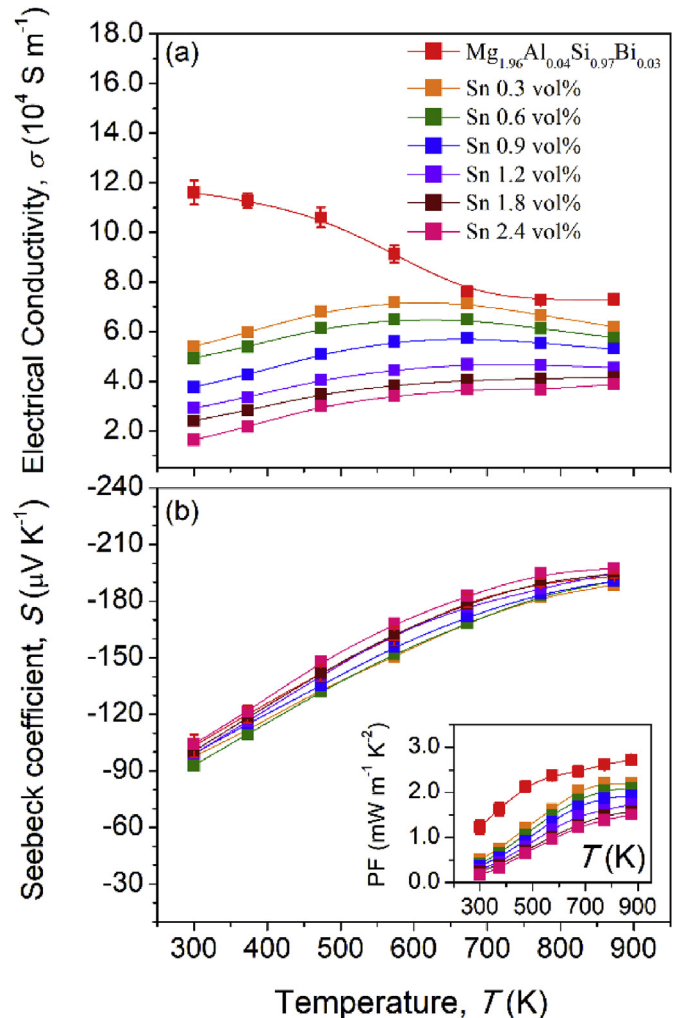
the electronic contribution (κ_{ele}) from κ_{tot}. The κ_{ele} was estimated using the Wiedemann-Franz law with L value of 2.00×10^{-8} V^2 K^{-2}. The κ_{lat} value of the 0.9 vol % Sn nanoparticle-embedded nanocomposite was relatively low, and those of the samples prepared at higher Sn contents were slightly higher (Fig. 5(b)). This trend originates from the existence of Sn nanoparticles, which increase thermal conduction because of the high thermal conductivity of the Sn metal (67 W m^{-1} K^{-1}), as well as the intensified phonon scattering at the interfaces between $Mg_{1.96}Al_{0.04}Si_{0.97}Bi_{0.03}$ and the Sn nanoparticles. In conclusion, the introduction of Sn nanoparticles has a limited effect in reducing the thermal conductivity.

The ZT values calculated from the measured σ, S, and κ_{tot} of all the samples are represented in Fig. 5(c). All the nanocomposites show lower ZT values (0.46–0.74 at 873 K) than the pristine sample (0.82 at 873 K) due to the decreased power factor despite the slight reduction in κ_{lat}. To investigate the trade-off relationship between the TE performance and the fracture toughness by the introduction of Sn nanoparticles, the dependence of ZT and the fracture toughness on the interface density was studied, and the results are shown in Fig. 6. As the interface density increases, the ZT value decreases gradually. However, it decreases rapidly at Sn contents higher than 0.9 vol %, which is caused by the aggregation of metal nanoparticles. To obtain the optimized values of ZT and fracture
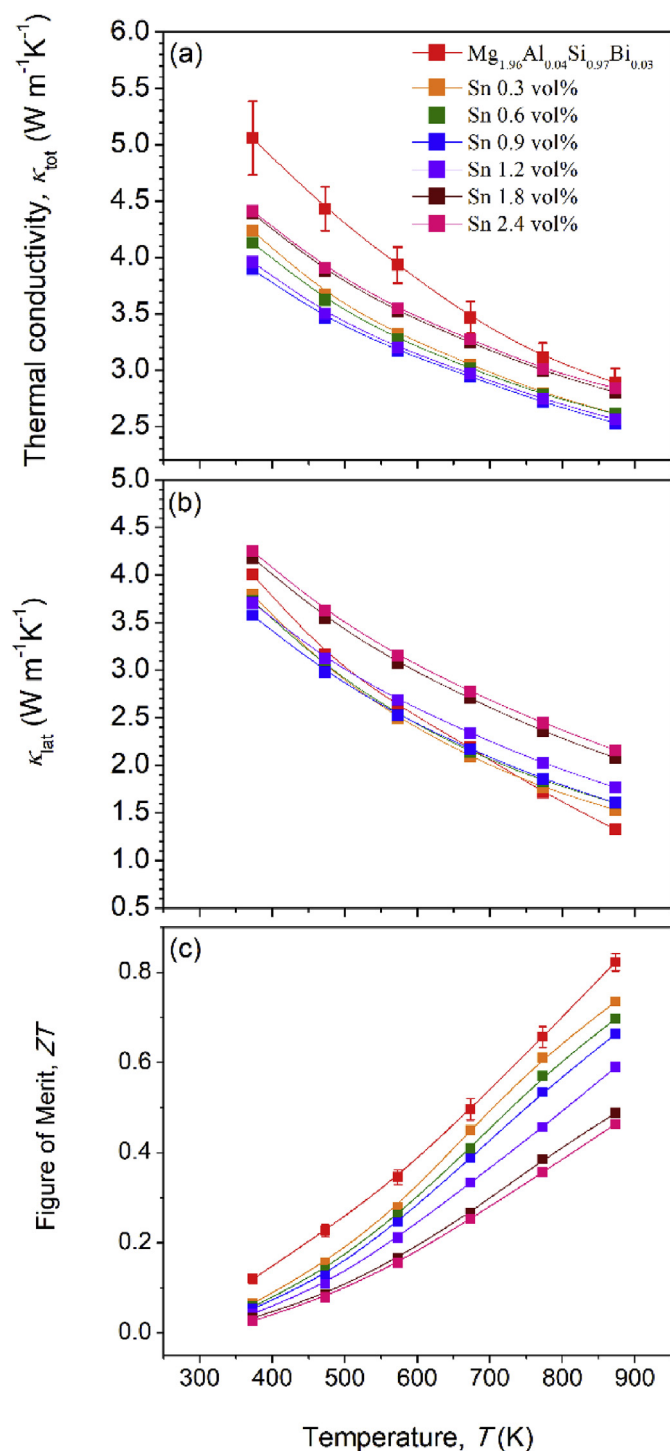
Fig. 6. Dependence of TE properties and fracture toughness on the interface density of Sn nanoparticle-embedded nanocomposites.

factor to overcome the trade-off relationship between TE and mechanical properties of Mg_2Si-based materials.

4. Conclusions

Sn nanoparticle-embedded $Mg_{1.96}Al_{0.04}Si_{0.97}Bi_{0.03}$ nanocomposites were synthesized by nanometal decoration and SPS processes. The fracture toughness of the nanocomposite increased by ~48% ($1.22\ MPa\ m^{1/2}$ at 2.4 vol % Sn nanoparticles) compared to that of the pristine sample due to the inhibition of crack propagation by the introduction of Sn nanoparticles with high toughness at the grain boundaries. However, the power factor value decreased because of intensified carrier scattering at the interfaces and the grain boundaries. Consequently, 0.9 vol % Sn nanoparticle embedded $Mg_{1.96}Al_{0.04}Si_{0.97}Bi_{0.03}$ exhibited optimized TE properties (ZT ~0.66 @ 873 K) and fracture toughness ($1.10\ MPa\ m^{1/2}$). Thus, precisely controlled nanophase design and synthesis are highly required to improve both the TE performance and the mechanical properties of Mg_2Si nanocomposite based TE materials.

Appendix A. Supplementary data

Supplementary data related to this article can be found at https://doi.org/10.1016/j.jallcom.2018.07.323.

References

[1] W. Liu, K. Yin, Q. Zhang, C. Uher, X. Tang, Natl. Sci. Rev. 4 (2017) 611–625.
[2] G. Kim, H. Lee, J. Kim, J.W. Roh, I. Lyo, B.W. Kim, K.H. Lee, W. Lee, Scr. Mater. 128 (2017) 53–56.
[3] R.D. Schmidt, X. Fan, E.D. Case, P.B. Sarac, J. Mater. Sci. 50 (2015) 4034–4046.
[4] P. Gao, I. Berkun, R.D. Schmidt, M.F. Luzenski, X. Lu, P.B. Sarac, E.D. Case, T.P. Hogan, J. Electron. Mater. 43 (2013) 1790–1803.
[5] Y. Gelbstein, J. Tunbridge, R. Dixon, M.J. Reece, H. Ning, R. Gilchrist, R. Summers, I. Agote, M.A. Lagos, K. Simpson, C. Rouaud, P. Feulner, S. Rivera, R. Torrecillas, M. Husband, J. Crossley, I. Robinson, J. Electron. Mater. 43 (2014) 1703–1711.
[6] B. Duan, P. Zhai, P. Wen, S. Zhang, L. Liu, Q. Zhang, Scr. Mater. 67 (2012) 372–375.

Fig. 5. Temperature dependences of (a) total thermal conductivity, (b) lattice thermal conductivity, and (b) ZT of Sn nanoparticle-embedded nanocomposites.

toughness, we plotted $\frac{K_{Ic}}{K_{Ic,\ Min}} \times \frac{ZT}{ZT_{Max}}$ factor as a function of the interface density (Fig. 6). Despite the lack of physical meaning in the factor, it is an important indicator of the TE applications because it is an implementation of the increase and decrease fraction of ZT and fracture toughness quantitatively. This factor has a maximum value for the 0.9 vol % Sn nanoparticle-embedded nanocomposite. These results suggest that the introduction of nanophases with well controlled compositions, dimensions, and sizes is an important
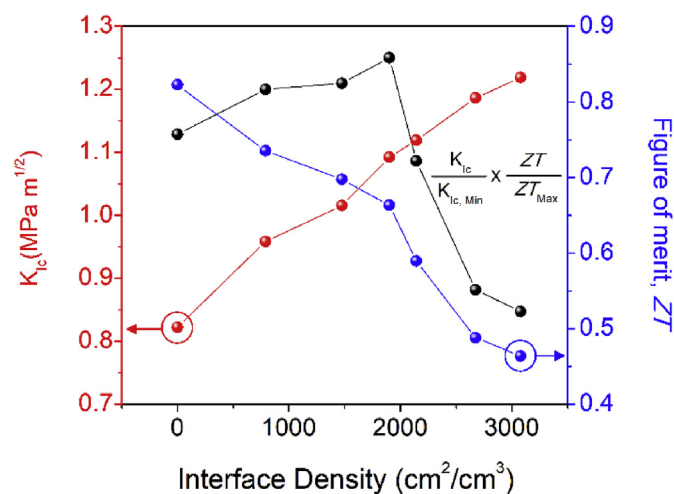
[7] B. Duan, P. Zhai, S. Ding, C. Xu, G. Li, L. Liu, P. Li, Q. Zhang, J. Electron. Mater. 43 (2014) 2115−2120.

[8] G. Rogl, A. Grytsiv, M. Gürth, A. Tavassoli, C. Ebner, A. Wünschek, S. Puchegger, V. Soprunyuk, W. Schranz, E. Bauer, H. Müller, M. Zehetbauer, P. Rogl, Acta Mater. 107 (2016) 178−195.

[9] K. Yin, X. Su, Y. Yan, H. Tang, M.G. Kanatzidis, C. Uher, X. Tang, Scr. Mater. 126 (2017) 1−5.

[10] G. Kim, H. Lee, J. Kim, J.W. Roh, I. Lyo, B.W. Kim, K.H. Lee, W. Lee, Ceram. Int. 43 (2017) 12979−12982.

[11] G. Kim, J. Kim, H. Lee, S. Cho, I. Lyo, S. Noh, B.W. Kim, S.W. Kim, K.H. Lee, W. Lee, Scr. Mater. 116 (2016) 11−15.

[12] S. Hwang, S.I. Kim, K. Ahn, J.W. Roh, D.J. Yang, S.M. Lee, K.H. Lee, J. Electron. Mater. 42 (2013) 1411−1416.

[13] K.H. Lee, H.S. Kim, S.I. Kim, E.S. Lee, S.M. Lee, J.S. Rhyee, J.Y. Jung, I.H. Kim, Y. Wang, K. Koumoto, J. Electron. Mater. 41 (2012) 1165−1169.

[14] Y. Lin, K.A. Watson, M.J. Fallbach, S. Ghose, J.G. Smith, D.M. Delozier Jr., W. Cao, R.E. Crooks, J.W. Connell, ACS Nano 3 (2009) 871−884.

[15] J.J. Kruzic, R.O. Ritchie, J. Am. Ceram. Soc. 86 (2003) 1433−1436.

[16] J. Boor, T. Dasgupta, H. Kolb, C. Compere, K. Kelm, E. Mueller, Acta Mater. 77 (2014) 68−75.

[17] L.S. Walker, V.R. Marotto, M.A. Rafiee, N. Koratkar, E.L. Corral, ACS Nano 5 (2011) 3182−3190.